preprint Fuel

Received 31 January 2021,
Accepted 13 April, 2021
https://doi.org/10.1016/j.fuel.2021.120973

preprint for final article published: *Fuel 300 (2021) 120973*

Fuel molecular structure effect on soot mobility size in premixed C_6 hydrocarbon flames

Shruthi Dasappa[a,b] and Joaquin Camacho *[a]

Soot formation in premixed laminar flames is examined for a canonical set of flames burning C_6 hydrocarbon fuels. Particle mobility size and flame temperature measurements are complemented by flame structure calculations using detailed flame chemistry. Specifically, the evolution of the detailed soot particle size distribution (PSDF) is compared for *n*-hexane, *n*-hexene, 2-methylpentane, cyclohexane and benzene at a carbon-to-oxygen ratio of 0.69 and maximum flame temperature of 1800 K. Under this constraint, the overall sooting process is comparable as evidenced by similar time resolved bimodal PSDF. However, the first inception of particles and the persistence of nucleation-sized particles with time are depend upon the structure of the parent fuel. For the given conditions, the fastest onset of soot is observed in cyclohexane and benzene flames and the observed evolution of the PSDF also shows that nucleation-sized particles disappear sooner in cyclohexane and benzene flames. Flame structure computations incorporating detailed chemistry show a clear connection between the early onset of soot particles as fuel specific routes to PAH formation are predicted in the pre-flame region of the cyclohexane and benzene flames. These observations illustrate the impact of alkane, alkene, cycloalkane and aromatic fuel structure on soot formation in premixed flames. Analysis of soot particle morphology by atomic force microscopy indicates that most of size distribution is composed of aggregates. Simple aggregate mobility diameter analysis shows the spherical assumption taken to interpret the mobility diameter does not impact the PSDF number density result but the inferred volume fraction for aggregates deviates by up to an order of magnitude depending on the morphology assumptions adopted.

1. Introduction

Soot formation is critical for optimization of internal combustion engines and other combustion applications [1]. Moreover, these emissions should be minimized as they eventually impact public respiratory health [2] and the environment [3]. Practical transportation fuels are complex mixtures of hydrocarbons and organics. A direct and complete kinetic description of real fuel combustion, including soot formation, is not feasible due to the variability and complex nature of the mixtures. Development of combustion chemistry models has relied upon studies of individual fuel components and simple mixtures serving as fuel surrogates. Premixed laminar flames are commonly employed to isolate chemical kinetic behavior of fuels from other aspects of the reacting flow [4,5]. Studies on soot formation in real fuel flames have been carried out in laminar premixed flames [6–8] but, the study of individual components could still provide important insights into fuel combustion chemistry and precursor formation. For example, examination of individual components could shed light on the behavior of real fuels containing species with overlapping size and molecular formula.

In the current work, soot formation behavior is investigated for a series of C6 hydrocarbons to explore effects of fuel structure ranging from the straight-chain alkane to the aromatic. Systematic studies of n-Hexane, 2-methylpentane, n-hexene, cyclohexane and benzene flames are carried out in a complementary experimental and modelling study. Soot formation is quantified here in terms of detailed particle size distribution functions measured by mobility sizing under well-defined boundary conditions. Flame structure calculations are used to characterize the flame temperature and chemistry with guidance from independent temperature measurements. The flame experiments are designed to isolate the fuel structure effect by constraining the flame temperature-time history to be nearly identical across all fuels studied. The gas-phase environment for soot growth is also constrained by using premixed flames with identical equivalence and C/O ratios. The series of flames acts a canonical set for soot formation among C6 fuels across the range of carbon bond structure and hydrogen saturation.

Fuel structure effects have been studied in sooting premixed flames of C6 fuels since classical studies of Hottel [9] and Whitcher [10]. Global soot formation was examined in premixed laminar flames of cyclohexane [11], hexane [12] and benzene [13,14]. Detailed behavior in premixed laminar flames has been examined in terms of soot particle size distribution function (PSDF) for hexane [15], cyclohexane [15] and benzene fuels [16–21]. The fuel structure effect on soot formation is more subtle in premixed flames than diffusion flames [5], but the aforementioned studies have systematically illustrated competing temperature, time and flame chemistry effects. The objective of the current work is to quantify the fuel structure effect on soot formation from alkane, alkene, cycloalkane and

---

[a] *Mechanical Engineering Department, San Diego State University, San Diego, CA USA*
[b] *Mechanical and Aerospace Engineering Department, University of California San Diego, San Diego, CA, USA*

aromatic fuels of the same carbon length under comparable conditions.

2. Materials and Methods

2.1 Experimental - The experimental configuration centers upon the burner-stabilized stagnation flame (BSS) configuration introduced by Abid and co-workers [22] to sample gas and aerosol samples under well-characterized boundary conditions. A custom flat-flame burner is used with a sintered bronze porous plug (5 cm diameter, 10 micron filter rating). Flow stagnation is induced by an aluminum plate mounted parallel to the burner surface to provide an explicit stagnation flow boundary condition for the sampling orifice ($D_{orifice}$ = 130 micron) embedded flush with the stagnation surface. The plate is a surface that accounts for flow stagnation induced by the aerosol sampling probe. This approach has been employed in several experimental [23–28] and computational [29–32] studies of incipient soot formation.

Table 1: Details of flame conditions studied

fuel name		X_{fuel}[a]	X_{O2}[a]	C/O	Φ	v_o[b] (cm/s)
n-hexane	n-C_6H_{14}	0.0748	0.325	0.69	2.19	4.57
		0.0716	0.328	0.65	2.07	4.39
2-methylpentane	i-C_6H_{14}	0.0748	0.325	0.69	2.19	4.57
		0.0716	0.328	0.65	2.07	4.39
n-hexene	n-C_6H_{12}	0.0748	0.325	0.69	2.07	3.85
cyclohexane	c-C_6H_{12}	0.0748	0.325	0.69	2.07	4.87
benzene	C_6H_6	0.0748	0.325	0.69	1.72	3.41
ethylene	C_2H_4	0.0748	0.325	0.69	2.07	7.46

Incipient soot formation in flames of C_6 hydrocarbons is examined in the set of atmospheric, fuel-oxygen-argon flames summarized in Table 1. For each flame condition, particle-laden flame products are drawn into the sampling probe at a series of sampling distances. Burner-to-probe separation distances, H_p , on the order of one centimeter are employed to sample the evolution of soot formation from the earliest inception stages to later growth stages. The set of flames are designed to have nearly identical temperature-time history for each fuel corresponding to a maximum flame temperature of 1800 K. Furthermore, the total C/O ratio of each fuel-O2 mixture is held fixed at C/O = 0.69 with two additional flow conditions introduced for the alkanes to compare Φ = 2.07 behavior. A comparable ethylene flame is also studied to demonstrate the C/O, C/H and fuel size effect. The adiabatic flame temperature for benzene is much greater than the other flames because the equivalence ratio is closer to unity. Thus, the cold gas velocity of the benzene flame is lower than the flow rate of the other fuels to match the 1800 K flame temperature constraint. The axial flame temperature profiles are measured with a Y_2O_3/BeO coated type-S thermocouple with radiation correction carried out from computed transport properties [33]. The bead diameter is approximately 0.3 mm after coating.

The flat flame burner is uncooled because of potential condensation of the fuel in the porous material. Without water cooling, however, the pores tend to sinter closed towards the center over time, thus modifying the local unburned gas velocity. For this reason, fresh porous material is always used to keep the flame radially uniform. A sheath of nitrogen shields the flame to prevent radial entrainment and diffusion of oxygen from ambient air. The C_6 hydrocarbon fuels, supplied by Sigma-Aldridge (ACS Reagent grade, 99% purity), are injected into the heated fuel line through an argon gas-assisted nebulizer for vaporization and mixing (Precision Glassblowing). The burner and fuel lines are thermostatically controlled at 400 K to prevent fuel condensation. Mass flow rates of oxygen, argon and nitrogen are measured by critical orifices and the flow of argon driving the fuel nebulizer is calibrated by a bubble displacement. Particle size distributions are determined by mobility sizing using a TSI 3080 SMPS (Electrostatic Classifier 3085 and UCPC 3080, AIM Software V.8.1) using a sample dilution technique developed to minimize probe artifacts [34–39]. The sample gas enters the probe through an orifice and is immediately diluted with a cold nitrogen flow to prevent particle losses. Limitations of the Cunningham slip correction cause particles below 10 nm to be overestimated by mobility measurements and thus a nanoparticle transport theory for small soot particles is employed [40,41]. A diagram of the experimental setup and typical BSS flames are included in the supplementary material.

Particle size and morphology analysis is carried out using a Nanoscope Multimode V atomic force microscope (AFM) on soot from the benzene and *n*-hexane flames. Soot samples are deposited by thermophoresis on freshly cleaved mica disks in a rapid insertion procedure. This substrate has a flat surface at the nanometer scale and is tolerant to heat. Particles are collected after insertion by swiping the substrate horizontally across the flame. A stepper motor maintains consistent swipe speed for an exposure time for each swipe of 12 ms. The samples are imaged immediately after collection to reduce instances of aging and oxidation in the ambient air.

2.2 Computational - The flame structure is computed by OPPDIF [42] to characterize the soot particle temperature time-history and gain insight into gas-phase flame chemistry. The pseudo one-dimensional formulation employed by OPPDIF has been shown to provide an efficient and fast solution to laminar premixed stagnation flames for characterization of detailed chemistry and particle processes [43,44]. Soot formation is not modeled in the current study, but analysis of soot precursor chemistry provides insight into the relative contributions of the C6 fuel structure to soot. The flame chemistry for the C_6 hydrocarbons is calculated with a reduced JetSurF mechanism [45] to be introduced below. OPPDIF allows for the calculation of the temperature and species profiles using only measured boundary temperatures. The temperature closest to the burner surface that can be measured is equal to one half of the thermocouple bead diameter (0.15 mm). The inlet temperature is extrapolated from the measured temperature profile immediately adjacent to the burner surface where temperature profile is roughly linear with respect to the distance, as one would expect in the pre-heat zone. The probe temperature is measured with a type K thermocouple embedded on the stagnation surface. The radiation corrected temperature profiles are compared to the independently computed temperature profile to validate the flame structure calculations.

The flame perturbation due to the sampling probe is accounted for in the OPPDIF code by introducing a stagnation surface at $x = H_p$ in the form of a zero velocity boundary condition [22]. For soot particles, the finite time in the flame is determined by considering the thermophoretic velocity which is driven by the significant temperature gradient at the stagnation plate. The thermophoretic velocity of the particle within the flame is calculated in the hard sphere and diffuse scattering limit [46]. The particle total velocity is determined by adding the computed thermophoretic velocity to the gas-phase convective velocity. The particle time is defined as the time interval for the particle (or precursors) to traverse from the calculated location of the sharp pre-heat temperature gradient to the location of the stagnation probe. The BSS method improves upon the temperature uncertainty induced by probe perturbation, but additional analysis is necessary to quantify the net velocity perturbation due to counter-acting flow stagnation and suction. BSS flames sampled under similar conditions were corrected previously [26,32] by an upstream shift in the probe position to compare with computational results. A brief analysis is carried out below to quantify systematic velocity perturbations based on previous probe perturbation analysis considering sampling distance, suction and orifice size effects.

Two combustion chemistry models are used for the C6 hydrocarbons currently studied. JetSurF 2.0 [45] is reduced here to only include oxidation for the given parent fuels along with the subsequent benzene formation chemistry. As discussed in the acknowledgements section, this reduction was carried out by the primary author of JetSurF to provide a more computationally efficient model for the fuel oxidation and benzene formation without compromising the validity of flame chemistry conclusions. The reduced JetSurF model, comprised of 1014 reactions and 175 species, includes details of the parent fuel combustion but polycyclic aromatic hydrocarbons (PAH) are not considered. To provide insight into PAH formation, a separate set of flame structure calculations are carried out using the CRECK C_1-C_{16} HT+Soot mechanism [47] in the reduced form introduced by Pejpichestakul and co-workers [48]. Soot formation processes are not currently considered so the sectional BIN reactions of the mechanism are neglected (244 species, 5880 reactions without soot BINS). The two chemistry models consider $_n$-hexene, cyclohexane and benzene combustion but $_n$-hexane chemistry only exists in JetSurF. Combustion chemisty of methylpentane is not readily available.

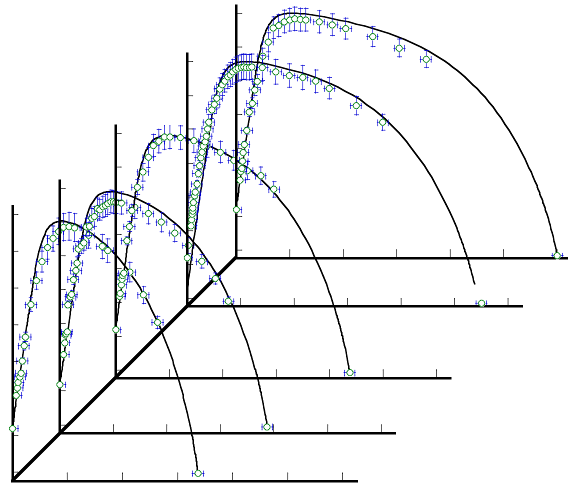

Figure 1: Measured (symbols) and simulated (lines) temperature profiles for the *n*-hexane flames at the centerline for the range of sampling locations, H_p.

3. Results and discussion

Measurements for each flame are taken at a series of Hp to track the evolution of the soot PSDF. The presence of the stagnation probe causes secondary stretch effects at the flame zone [22,49] and a drop in velocity and temperature downstream at the probe boundary. The local temperature is measured here to characterize these flame structure effects on the current burner-stabilized stagnation flames. This characterization is crucial as local temperature is the dominant parameter which governs flame chemistry and soot formation processes [5,50]. A comparison between the measured and computed (JetSurF) axial temperature profile is shown in Fig. 1 for the *n*-hexane flames. Even though the flow rates do not change, each Hp condition provides a new boundary condition which requires its own flame structure computation. The temperatures at the inlet and stagnation plate boundaries are used to solve the energy equation for a temperature profile solution based on the boundary values. The agreement between the radiation corrected measurements and the simulated temperatures is within the thermocouple position uncertainty (± 0.3 cm) and the temperature measurement uncertainty (± 70 K around the peak temperature region). The temperature profiles for the other fuels studied are similar at a series of sampling distances.

A comparison between measured and simulated (JetSurF) axial temperature profiles is shown in Fig. 2 for all fuels studied. The temperature profiles overlap to a large extent but differences in the pre-heat and post-flame are observed. The micrometer stage has positional precision of 50 micron but the thermocouple measurements are assigned positional uncertainty of ± 300 micron to account for uncertainty in the burner surface position and uncertainties stemming from variation in wire tension and vibrations. The bottom plot of Fig. 2 expands the x-axis to emphasize the sharp temperature gradient in the pre-heat region where several thermocouple measurements are taken. The calculated benzene flame temperature peaks slightly sooner due to faster fuel kinetics but the post-flame region is colder due to the lower cold gas velocity. The model solves the energy equation without the measured temperature profiles as an input. Thus, agreement between radiation corrected measurements and the computed temperature profile is an indication of the performance of the underlying combustion chemistry model. Uncertainty within the simulated local flame temperature along with the resulting Arrhenius reaction kinetics and species transport can be defined with this information. In addition, the agreement between the measurement and computation confirms that the flame conditions are comparable, and that sooting behavior can be observed under similar local temperature.

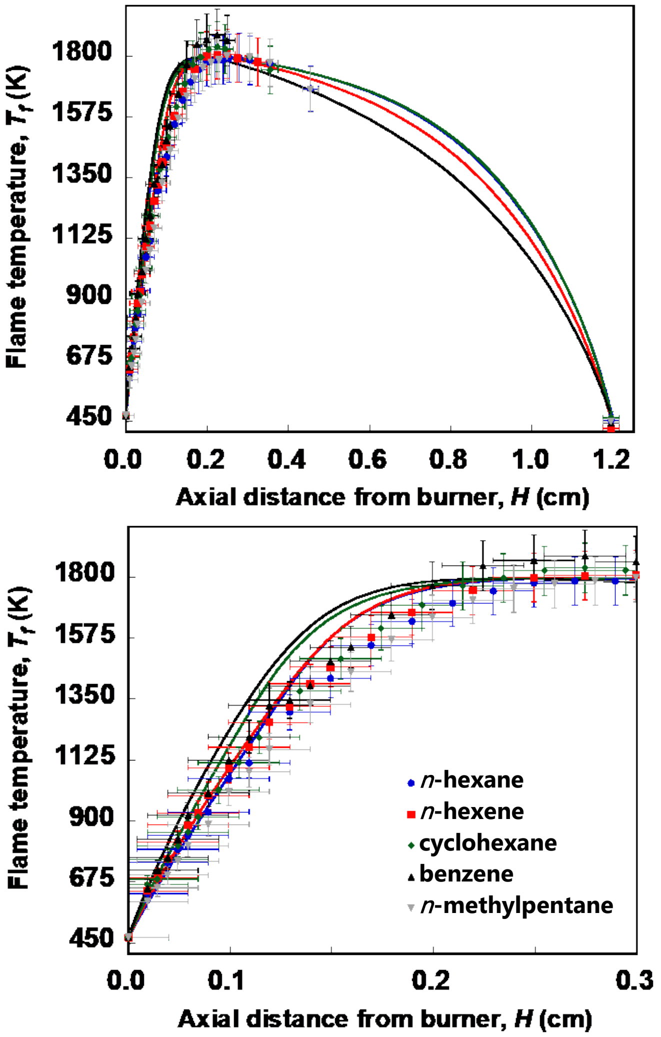

Figure 2: Measured (symbols) and simulated (lines) axial temperature profiles for all flames at the centerline with H_p = 1.2 cm (top) and the same profile with the flame-zone expanded on the x-axis for greater clarity (bottom).

Detailed sooting behavior is examined in terms of the evolution of particle mobility size distributions for the sooting flames of C6 hydrocarbons. The PSDF evolution from the onset of nucleation size particles to later growth stages is summarized in Fig. 3 for the straight chain and branched chain isomers of hexane (C_6H_{14}). Local flame temperature and C/O ratio dominate the global sooting behavior of premixed flames, thus the constrained peak flame temperature and C/O ratio will isolate the fuel structure effect between the two isomers of hexane. At the early stage of soot formation, newly formed particles burst into the lower end of the measurable size window at 2.4 nm. These particles grow in size, producing a shoulder in the PSDF, which grows into a log-normal distribution at larger burner-to-stagnation surface separations. Meanwhile, particle inception persists well into the large separation distances as evidenced by the observed PSDF consisting of a prominent nucleation-sized mode at all sampling positions.

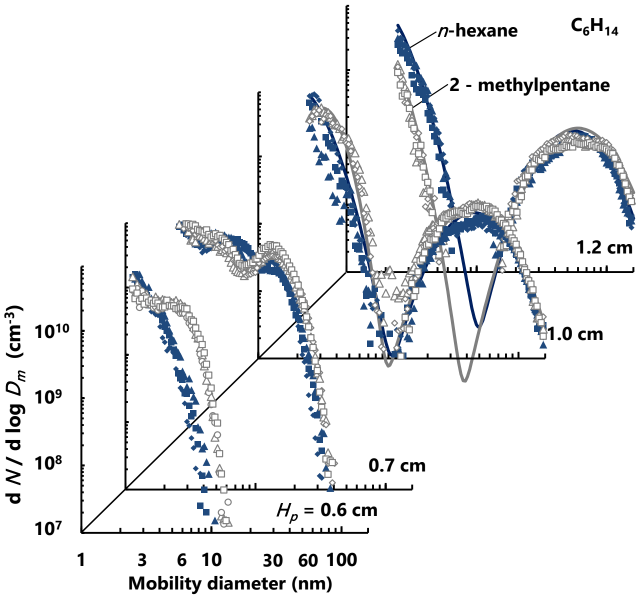

Figure 3: Measured PSDFs for n-hexane (filled symbols) and 2-methylpentane (open symbols) flames. Bi-modal log-normal distributions (solid lines) are fit to the PSDF at H_p = 1.0 and 1.2 cm to highlight nucleation size particles which persist late in the flame.

Overall, the competition between the nucleation and growth processes of soot is similar across the two hexane isomers with the differences being only quantitative and subtle. As Fig. 3 shows, the onset of soot is slightly delayed in the n-hexane flame compared to the 2-methylpentane flame, but during the mass and size growth stages, and PSDFs become less distinguishable. At the largest separation distance probed (H_p = 1.2), the lognormal part of the distributions nearly overlap each other, whereas the nucleation mode of the PSDF exhibits reproducible and subtle differences. The relative trend in particle inception and overall PSDF characteristics between branched and straight chain isomers observed in Fig. 3 has also been observed in previous observations of sooting C_4 premixed BSS flames [25]. In the study of C_4 fuels, delayed soot onset and smaller particle size distributions were observed in the straight chain isomers when compared to the branched chain fuel. The present comparison between methylpentane and n-hexane shows a similar trend, but this fuel effect may be reduced by the extended carbon chain of C_6H_{14} which exists in both isomers.

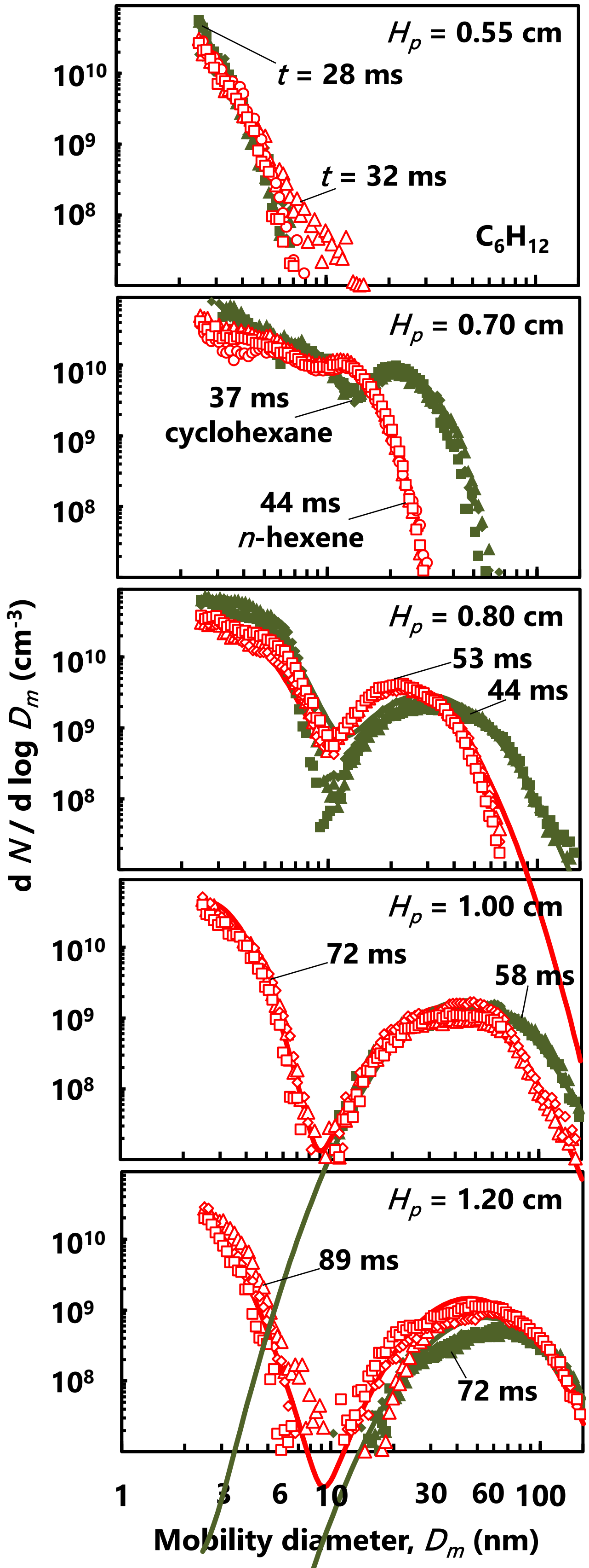

Figure 4: Measured PSDFs for cyclohexane (filled symbols) and n-hexene (open symbols) flames. Bi-modal log-normal distributions (solid lines) are fit to each PSDF.

For the previous isomers, the evolution of incipient soot can be directly compared in terms of particle residence time for each Hp because the boundary conditions, flow rates and resulting flame structure are the same. A similar comparison for the C_6H_{12} isomers (cyclohexane and *n*-hexene) is made but the comparison is not as direct because lower flow rate of the n-hexene flame causes longer particle times for the given sampling locations. The adiabatic flame temperature of n-hexene is greater than cyclohexane. Thus, the constraint of C/O = 0.69 and 1800 K maximum flame temperature is satisfied for cyclohexane and the other fuels by controlling the cold gas velocity of the BSS flame. The development of the PSDF in terms of both sampling location and particle time is summarized in Fig. 4 for both C_6H_{12} isomers. Particle inception occurs for each isomer at a sampling location in the vicinity of the lowest sampling distance reported. The burst of nucleation-sized particles observed at H_p = 0.55 cm does not correspond to the precise location of the rapid gas-to-particle conversion but the PSDF clearly corresponds to the earliest soot growth stages. The evolution of the PSDF is similar for the branched alkane, straight alkane, straight alkene and cycloalkane analogs of C_6. In all the flames studied, the onset of nucleation-sized particles is followed by a bimodal PSDF due to persistent soot particle inception. In addition, the trough between the nucleation and growth particle sizes is roughly 10 nm in each flame which may indicate that the particle inception processes are similar among these flames [31].

Quantitative differences in detailed sooting behavior between the C_6H_{12} isomers (cyclohexane and n-hexene) are more prominent than the alkane isomers (n-hexane and methylpentane) previously discussed. The PSDF growth summarized in Fig. 4 indicates that soot from n-hexene forms later and grows slower than cyclohexane soot. For example, the median mobility diameter of the PSDF is 45 nm for both of the C_6H_{12} flames at Hp = 1.0 cm. However, it took nearly 20% less time for the median diameter to reach this size in the cyclohexane flame. Another striking difference in the soot PSDF of the C_6H_{12} isomers is the relative intensity of the nucleation-sized mode within the PSDF. Particle inception persists late for both flames but the nucleation-size particles become undetectable after 70 ms in the cyclohexane flame. Under comparable composition and flame conditions, the relative early end to nucleation in the cyclohexane flame is attributable to fuel specific chemistry and soot formation processes. Chemical pathways are examined below for insight into the observed particle inception behavior in cyclohexane flames. Further fuel specific details of soot formation processes such as the persistence of the nucleation-sized mode require further complementary experimental and modeling investigation, and this will be left to future work.

The above comparisons for evolution in PSDF with increasing sampling height and particle time do not account for probe perturbations to the flame structure. Previous analysis for probe perturbations in BSS flames [26,32] showed that computed PSDF match closer to distributions measured by aerosol probe suction if an upstream shift is applied to the experimental PSDF. A typical upstream shift in the range of 1-2 mm was applied to match benchmark sooting flame PSDF data depending on the burner boundary inlet velocity, sampling distance, sampling pressure drop and orifice size. The inlet velocity of the unburned mixture is on the order of 9 cm/s for the C_6 fuels currently studied. Extrapolating the previous factorial analysis [32] for probe perturbations gives an estimated upstream shift such that the experimental sampling distance, H_p, corresponds to (Hp – 0.19 cm) for computed PSDF. The corresponding reduction for particle time is t - 10 ms. The unburned mixture inlet velocity for the C_6 flames has a range of 34% between the slowest and fastest flows and the resulting difference in upstream shift is predicted to be less than 0.01 cm across this range. The range of sampling distances currently employed ($0.55 < H_p < 1.2$ cm) corresponds to an upstream shift of 0.15 cm at the smallest distance and 0.20 cm at the largest distance. These estimations of upstream shifts systematically effect all the probe-obtained measurements uniformly. As such, comparisons of the measured PSDF can be made across the C_6 fuels with minimal impact from the systematic probe perturbation.

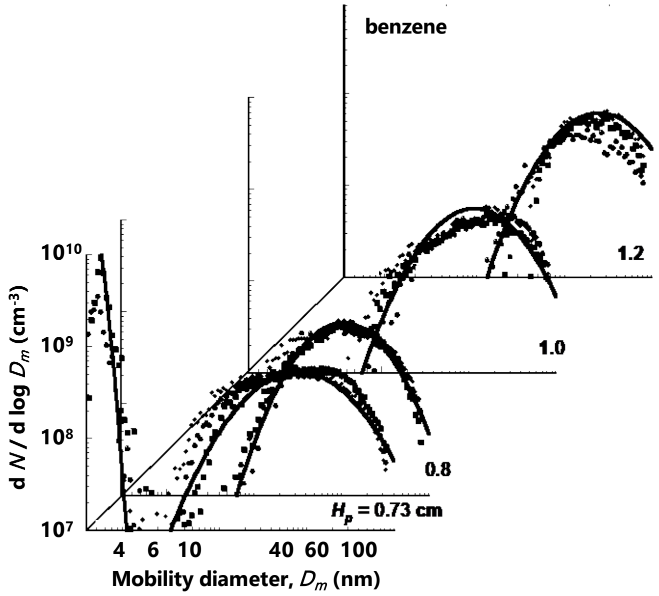

Figure 5: Measured PSDFs for benzene (filled symbols) flames. Bi-modal log-normal distributions (solid lines) are fit to each PSDF.

The evolution of soot PSDF in the benzene flame is summarized in Fig. 5. The development of the size distribution does not follow the other fuels at the given sampling locations. The smallest sampling distance that could be probed in a stable manner is more limited in benzene than the other flames because the benzene flame is more sensitive to heat loss to the stagnation probe. As shown in Fig. 2, the axial temperature profile for the benzene flame peaks at 1800 K but the post-flame region is weaker than the other flames due to the lower cold gas velocity. The benzene flame is significantly disturbed by the sampling plate at H_p = 0.7 cm because the sharper temperature gradient of the post-flame causes more heat loss to the probe. The sampling distance corresponding to the burst of soot inception cannot be directly accessed but Fig. 5 shows that the bimodal distribution exists at the lowest stable sampling distance. Nucleation size particles become undetectable after H_p = 0.8 cm in the benzene flame and the PSDF transitions to a single log normal mode of larger particles. The median mobility particle size is significantly greater in the benzene flames compared to the other C_6 fuels.

Besides affecting the temperature profile, the lower cold gas velocity in the benzene flame also increases the residence time that particles undergo at the given sampling distances. The effect of longer residence time may contribute to the end of nucleation and larger particle size in the benzene flames. Additional information on the PSDF is gained from AFM images of particles deposited in the vicinity of the flame zone. An AFM image of particles deposited from the benzene flame is shown in Fig. 6. The stagnation plate is located at Hp = 1.0 cm for this deposition experiment, but the mica substrate is inserted at the flame zone to (H_p = 0.7 cm) to probe the particle size and morphology at the earliest stages. The AFM image shows primary particles and small aggregates in a similar size range of the PSDF from the other fuels. This is a confirmation that evolution of soot formed in the benzene flame also begins with a bi-model distribution including a mode of nucleation sized particles.

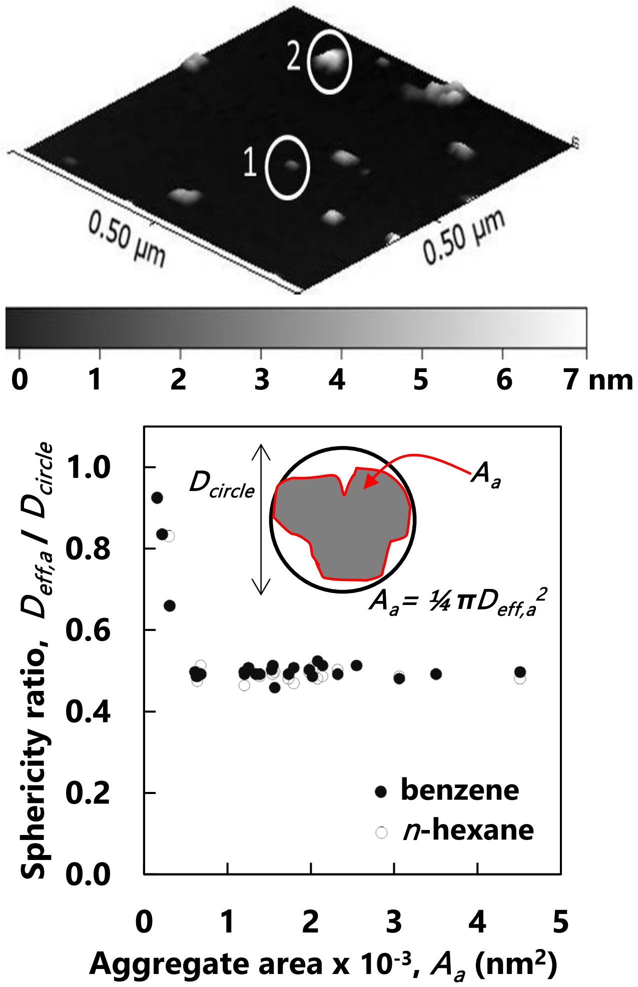

Figure 6: AFM image of incipient soot particles from the benzene flame deposited in the vicinity of the flame front (top) and sphericity ratio vs. cross-sectional particle area based on AFM images of particles deposited from the n-hexane (H_p = 1.0 cm) and benzene flames (H_p = 0.7 cm, bottom). Particle 1 in the AFM image is a primary particle with a diameter of approximately 5nm and particle 2 is an early aggregate with a diameter of approximately 7nm.

Morphology observations from AFM are also used here to gain insight into the measured mobility diameter. Interpretation of the measured particle mobility requires knowledge or assumptions of the particle morphology. The simplest assumption is for spherical morphology and mobility in the electric field can be characterized by a modified Stokes drag expression for a sphere of diameter Dm [51]. For aggregates, an effective diameter, $D_{eff,a}$, can be defined based on the projected cross-sectional area of the aggregate, A_a , via $A_a = \pi/4\ D_{eff,a2}$. This effective diameter can be considered to be the mobility diameter for aggregates in the free-molecular regime [52,53]. The sphericity ratio, Ψ , is used here as a measure of particle morphology as follows:

$$\Psi = D_{eff,a} / D_{circle} \qquad (1)$$

where D_{circle} is the smallest diameter of a circle enclosing the perimeter of the particle in the AFM image. The particle cross-sectional area is determined by AFM for a set of particles from the n-hexane and benzene flames (25 particles each) and the result is shown in Fig. 6 in terms of the sphericity ratio. These flames represent the highest and lowest level of hydrogen saturation in fuel molecular structure for the C_6 hydrocarbons, yet the soot particle morphology (in terms of sphericity) is not significantly different. A deviation from spherical particle morphology is observed for particle size on the order of 10 nm (area ~ 100 nm^2). Similar sphericity ratio was reported for incipient soot from premixed ethylene flames at comparable equivalence ratio and flame temperature [54].

Global sooting properties such as total soot volume fraction, F_v , can be determined for each flame by integrating the PSDF over all particle sizes measured (D_m > 2.4 nm). The above discussion of mobility diameter has a strong impact on the volume fraction inferred from mobility size distributions [26,55]. Four simple models are applied here to compare the connection between measured mobility size and volume fraction. The first model assumes the particle mobility is a related to the Stokes Drag expression modified for extrapolation to spheres in the free-molecular regime. This is the model applied to the measured PSDF reported in Figs. 3-5. The second and third model use the framework introduced by Lall and Friedlander [56] for aggregates under simplifying assumptions. The key assumptions are that all aggregates in the distribution are characterized by a single primary particle size, the primary particle size corresponds to the free molecular regime, the total surface area and volume corresponds to the sum of the individual primary spherical areas and volumes (no necking), and the fractal dimension is low enough that all of the particle surface area is exposed to gas collisions. These assumptions do not describe the polydisperse primary particles and necks that exist in incipient soot aggregates, but the analysis provides a lower limit for volume fraction inferred from the measured mobility diameter. The second model assumes a single primary particle size of D_p = 5 nm and the third model uses D_p = 20 nm. These limiting cases for primary particle size correspond to the range of primary particles reported for incipient soot in premixed laminar flames under similar conditions [54,57]. The fourth model is a simple correction to the spherical volume fraction by a factor corresponding to the measured sphericity, Ψ = 0.5. This results in a reduction in the spherical volume fraction by a factor of 8.

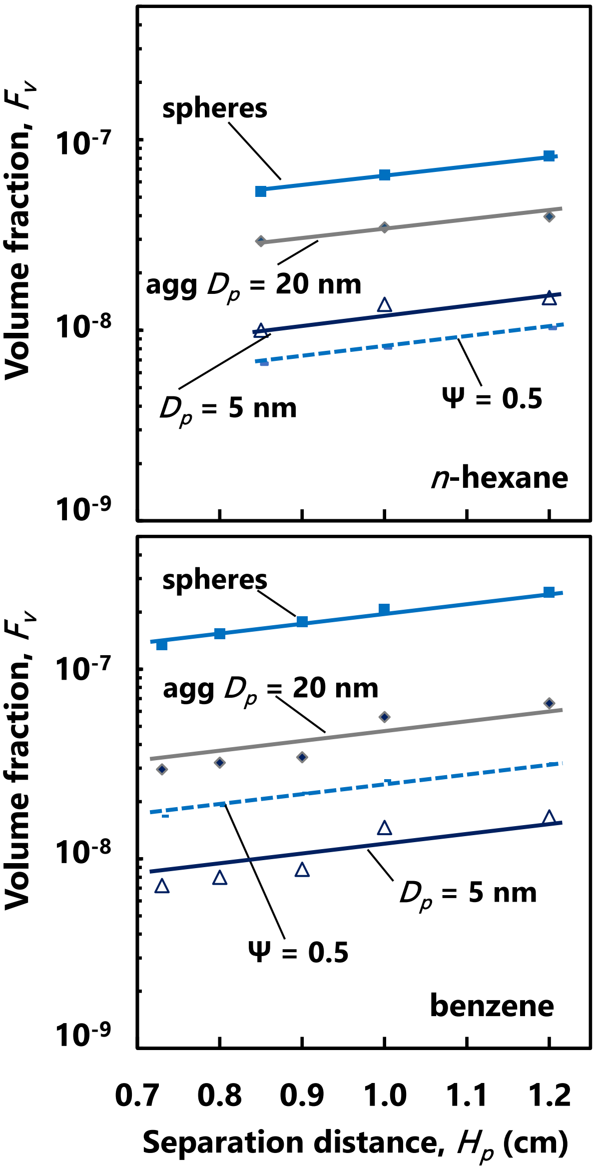

Figure 7: Volume fraction derived from the measured mobility size distributions under the four morphology models for PSDF sampled from the n-hexane (top) and benzene (bottom) flames. Lines are drawn to guide the eye.

The Nanoparticle Aggregate Mobility Analysis Software Module is invoked in the mobility sizing software to apply the aggregate assumptions described above. An example volume weighted PSDF is included in the supplementary material to highlight the significant reduction in volume distribution when aggregate morphology is considered. The connection between the measured mobility diameter and the interpreted aggregate size distribution is also included in supplementary material. A summary of results from the morphology models is shown in Fig. 7 in terms of soot volume fraction. The PSDF measured at each separation distance spans 2.4 < D_m < 160 nm when the spherical assumption is applied but application of the aggregate analysis limits the smallest mobility size to the chosen primary particle diameter. The PSDF also extend outside of the measurement window for the largest PSDF so the volume fraction is derived from a lognormal fit to the volume weighted PSDF as discussed previously [27]. Precise interpretation of this range of sizes requires consideration in evolution in particle morphology with increasing particle size. For example, the spherical assumption may be reasonably accurate for the nucleation-sized mode reported in Figs. 3-5 but the transition from coalescence to aggregate growth occurs for soot at particle size ~ 10 nm [58,59].

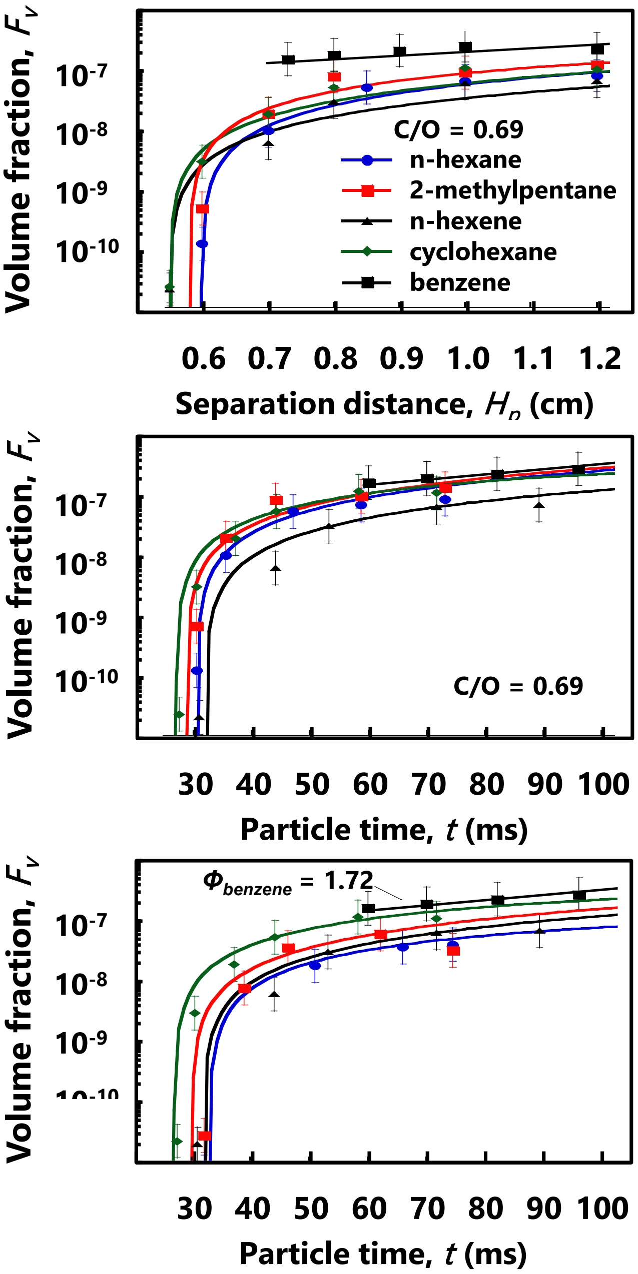

Figure 8: Measured volume fraction based on the spherical particle assumption for all flames studied in terms of space (top) and particle time (middle). Also, shown is additional methylpentane and n-hexene flames to match the Φ = 2.07 condition (bottom). Lines are drawn to guide the eye.

As expected, the spherical particle assumption results in volume fractions much larger than the models considering aggregate morphology. For an aggregate incorrectly assigned the spherical assumption, the mobility diameter is approximated by the diameter of a circle enclosing the fractal shape of the aggregate along with the corresponding empty space. The simple aggregate models applied here begin to account for the effective diameter corresponding to the actual collision area of the soot aggregates. The D_p = 5 nm likely over-compensates for the soot aggregate mobility diameter because soot primary particles undergo surface growth over time to form larger primary particles and necks. The D_p = 20 nm is a more reasonable size to represent the average primary particle size of larger soot aggregates for which the soot volume fraction is weighted towards. The simple correction based on the sphericity is based on measured particle morphology, but the application of a single correction factor is over-simplistic and requires more extensive morphology and/or mass characterization. Nonetheless, the current analysis indicates that the soot volume fraction inferred from measured mobility size distributions based on the spherical assumption are over-predicted by up to an order of magnitude. Methods first applied to diesel soot [60] have recently been extended to incipient soot in the earliest growth stages to more precisely quantify the effect of aggregate morphology and interpretation of the mobility diameter [26,55,61].

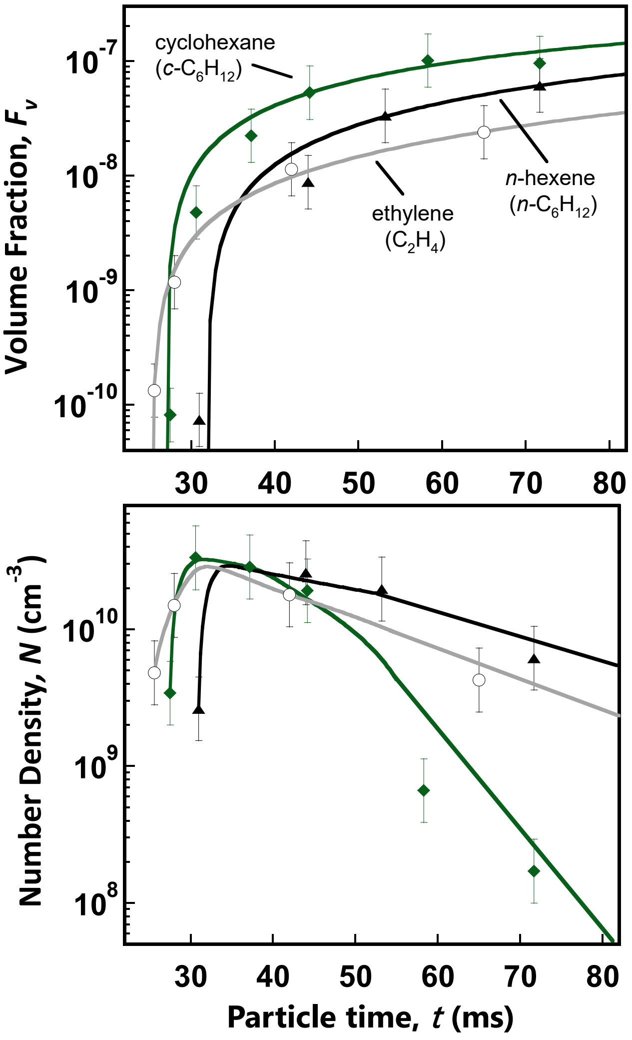

Figure 9: Measured volume fraction based on the spherical assumption for cyclohexane, n-hexene and ethylene flames (top) and number density (bottom). Lines are drawn to guide the eye.

The spherical particle assumption is taken to compare measured soot volume fraction for a consistent basis among soot formed from the current range of parent fuels. The above sphericity measurements provide evidence that the deviation from spherical shape is comparable for incipient soot formed in n-hexane and benzene flames. A relative comparison of volume fraction among the current set of flames is possible regardless of the morphology assumption employed because the temperature-time history and flame stoichiometry are comparable. As such, differences in PSDF could be attributed primarily to the parent fuel as long as the same morphology model is applied. The soot volume fraction under the spherical particle assumption as a function of burner-to-probe separation distance, Hp, is shown in Fig. 8 for all C_6 hydrocarbon flames studied. Each BSS flame is sampled within the same range of Hp as shown in the top plot of Fig. 8. However, the residence time that soot particles experience in the post-flame region varies for each flame due to the contrasting flow rates. The middle plot of Fig. 8 shows that the global sooting behavior clusters closer together for all flames on the basis of residence time. This is expected because the particle residence time is a more fundamental scale for tracking the evolution in size distribution than the sampling height. The onset of nucleation occurs 25 ms after the flame zone and the total soot volume fraction reaches 10^{-7} after 70 ms. The time development of detailed PSDFs and global properties is similar between the given C_6 hydrocarbon flames. This observation follows the established conclusion that global sooting behavior is dominated by flame temperature and C/O ratio in premixed flames rather than the structure of the fuel. However, comparisons of the fuel structure impact can be made between the given C_6 hydrocarbons on a more quantitative level if the timescale of soot formation is established. The evolution in volume fraction results in lower soot production for the n-hexene flames on the basis of C/O = 0.69. The volume fraction relative to the alkane flames (Φ = 2.19, C/O = 0.69) may be explained by the lower equivalence ratio of the n-hexene flames (Φ = 2.07, C/O = 0.69). The volume fraction relative to benzene and cyclohexane may be explained by chemistry pathways to soot precursors, a hypothesis explored below.

The final soot volume fraction under the spherical assumption is the greatest in the benzene flame for the given conditions. This conclusion is expected based on the aromatic structure of benzene but the difference in final volume fraction observed between the other premixed BSS flames is only a fine detail. For the same C/O ratio, hexane, methylpentane and cylcohexane flames approach the final soot volume fraction of benzene flame if the trend with time is extrapolated. The detailed PSDFs also show that the final median diameter is 50-60 nm for each flame with soot from the benzene flame consistently being the largest. A comparison of volume fraction on the basis of equivalence ratio is shown in the bottom plot of Fig. 8 for Φ = 2.07. On this basis of fixed equivalence ratio, the volume fraction of soot increases with the C/O ratio, again, with a minor deviation of n-hexane which lies in between the alkane flames. In this case, the branched alkane flame may be slightly more favorable to soot formation than the straight chain alkene and alkane flames.

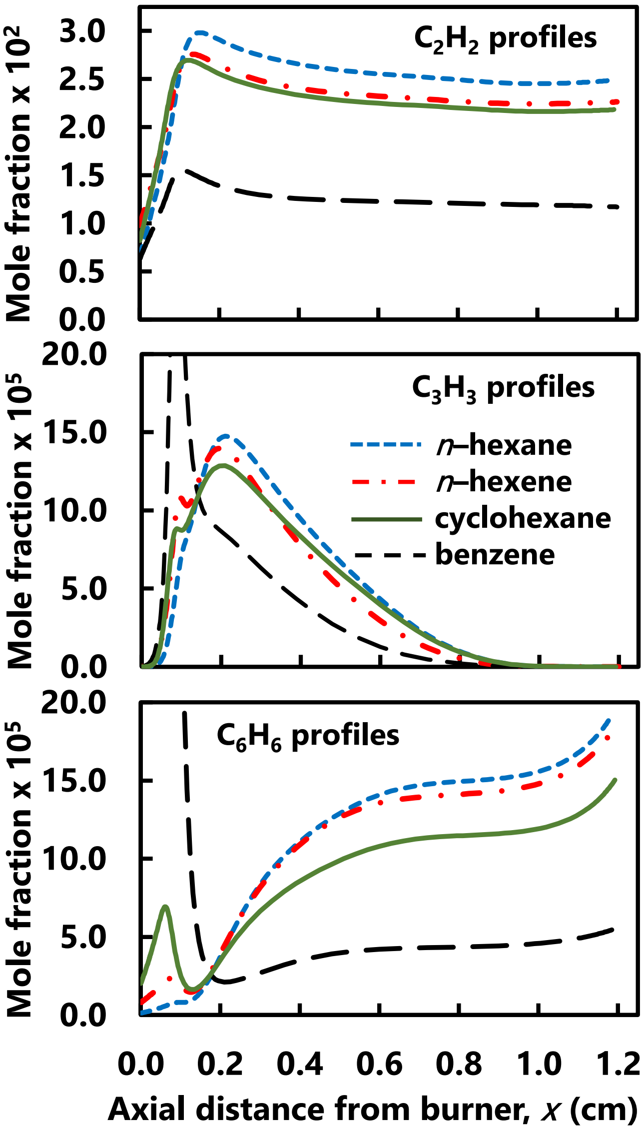

Figure 10: Computed profiles at H_p = 1.2 cm for acetylene (top), propargyl radical (middle) and benzene (bottom) for C_6 fuels included in JetSurF.

The impact of the parent fuel structure can be examined further if both the equivalence ratio and C/O ratio are identical. This comparison is shown for in Fig. 9 for the cyclohexane, *n*-hexane and an ethylene flame (C_2) in terms of the soot volume fraction and number density. The ethylene flame is similar to the BSS flame reported previously [22] with the flame temperature slightly decreased to match the current study. On the basis of identical C/O and C/H ratio, the impact of the parent fuel structure is seen in the premixed flames in terms of contrasting final soot volume fraction, number density and nucleation time. The hierarchy of the soot volume fraction resembles the relative trend observed in non-premixed flames where aromatic structures and higher carbon number increase soot. Ethylene has the lowest carbon number and cyclohexane is a hydrogen saturated ring. The number density of the cyclohexane flame shown in Fig. 9 is relatively small because nucleation size particles stop forming over time in the cyclohexane flames as discussed above.

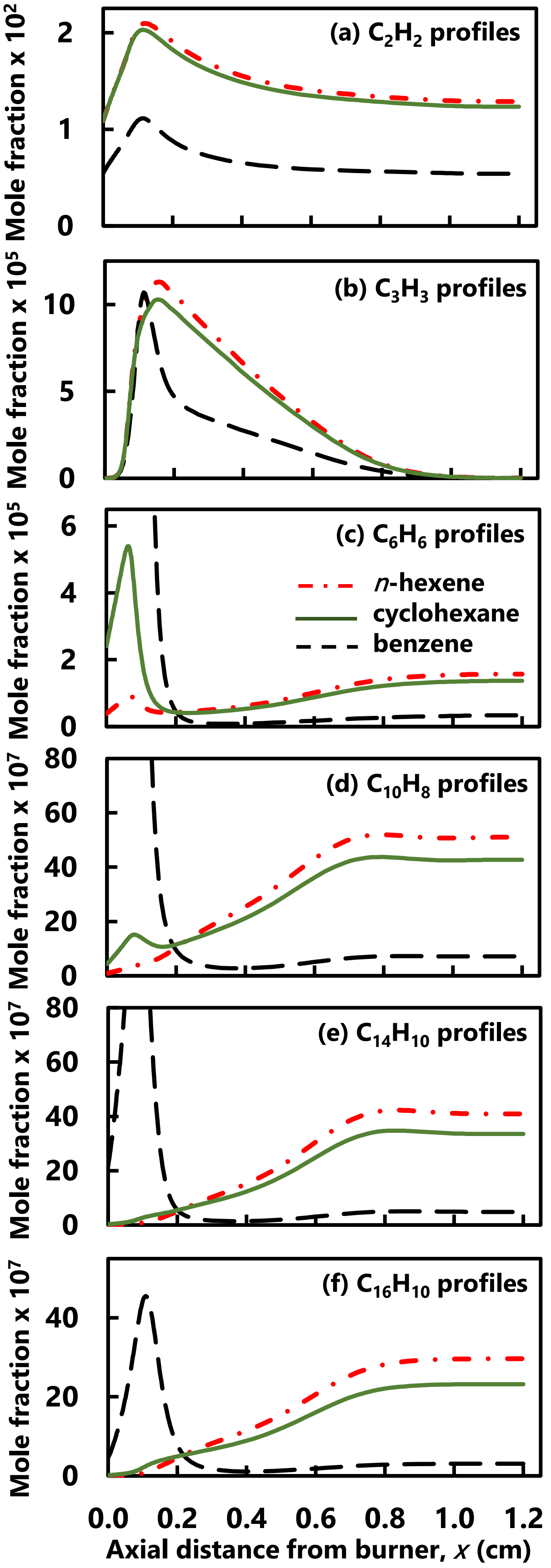

Figure 11: Computed profiles H_p = 1.2 cm for acetylene (a), propargyl radical (b), benzene (c), $C_{10}H_8$ (d), $C_{14}H_{10}$ (e), $C_{16}H_{10}$ (f) for C_6 fuels included in the CRECK PAH model.

Detailed sooting characteristics such as the soot inception time and persistence of inception with time can be established if the particle residence time is known. The persistence of new particle formation can be inferred by the detection of a nucleation-sized mode in the detailed PSDF. The range of sampling distances (particle time) where this small particle mode is present varies across the flames. The cyclohexane and benzene flames stop forming incipient soot 70 ms after the flames zone. With factors such as flame temperature, C/O ratio and residence time eliminated, this indicates that soot precursor and monomer depletion occur more readily in the aromatic and alkane ring fuels. However, the precise process in the benzene and cyclohexane flames which causes this behavior is unknown. This behavior has been reported by Echavarria and co-workers [18] for PSDFs in benzene premixed flat flames and was explained by consumption of aromatic precursors in the oxidation zone. The disappearance of nucleation-sized particles could also be plausibly related to local flame temperature and larger surface area rather than a direct consequence fuel-specific chemistry.

Previous experimental and modeling studies have shown that competing kinetic processes of soot formation can be related to features of the bi-modal PSDF [30,31,36]. The transition from bimodal back to unimodal must also be included in soot formation models for cases such as cyclohexane and benzene where precursor depletion occurs and soot inception is no longer present. The time at which the onset of soot nucleation occurs can also be determined in PSDFs from the current BSS flames. The relative order in which nucleation begins may reveal insight into the fuel structure effect on soot precursor formation. Differences are observed among the C_6H_{12} and C_6H_{14} isomers, for example. All measured PSDF indicate particle inception occurs approximately 30 ms after the flame front, but the relative PSDF magnitude at this stage indicates that cyclohexane flames lead to faster soot inception. The inception region of the benzene flame could not be probed with the current method but non-intrusive experimental techniques employed by Minutolo and co-workers [62] have indicated incipient particles are formed in the oxidation region of laminar premixed benzene flames. The competing kinetic processes leading to inception of soot are linked to the underlying gas phase chemistry in a manner that is not completely understood. The formation of aromatic precursors is considered a rate-limiting step for soot formation and the onset of soot inception may be tied to the fuel specific chemistry leading to aromatic formation.

Available combustion chemistry models incorporating detailed mechanisms of the current C_6 hydrocarbons are used for insight into fuel-specific soot formation behavior. Species profiles of gas-phase soot precursors are analyzed for the *n*-hexane, *n*-hexene, cyclohexane and benzene flames. Chemistry for 2-methylpentane is not readily available but the behavior relative to *n*-hexane may be similar to the relative behavior reported for *i*-butane and *n*-butane fuels under comparable conditions [45]. The faster nucleation time and greater final volume fraction in methylpentane discussed above may be influenced by greater benzene formation in the pre-flame and post-flame regions as observed in the previous butane study. The JetSurF gas-phase kinetic model does not extend to PAH formation. As such, the sensitivity of soot precursor formation to the fuel structure is evaluated based on production of acetylene, propargyl radical and benzene with computed axial species profiles shown in Fig. 10. The hexane flame is predicted to form the highest concentrations of acetylene, propargyl and benzene. This could be explained by the higher equivalence ratio of the alkane flames which is required to match the C/O = 0.69 constraint. In a similar fashion, the lowest precursor concentrations in the post-flame region are predicted for the benzene flame due to a lower equivalence ratio. Based on the computed precursor profile, the majority of soot precursors for the benzene flame form in the pre-heat zone. Besides the obvious presence of benzene, propargyl is much higher in the pre-heat zone of the benzene flame than the other fuels. A prominent peak of benzene formation is also predicted in the pre-heat zone of the cyclohexane flame. The onset of particle inception is fastest in the cyclohexane flame and the pre-flame peak of benzene production shown in Fig. 10 may influence this detailed sooting behavior. The predicted benzene formation in the pre-heat zone allows for a possible pathway to soot which starts before the flame front. Pre-flame aromatic production is an exceptional case which does not exist in the classical mechanism of soot formation in premixed flames. It is well established that local flame temperature and acetylene production in the post flame are the main factors controlling soot precursor formation thus the parent fuel structure is only of secondary importance [5,63]. In this case, the fuel structure of cyclohexane has a primary impact in a manner not conventionally considered.

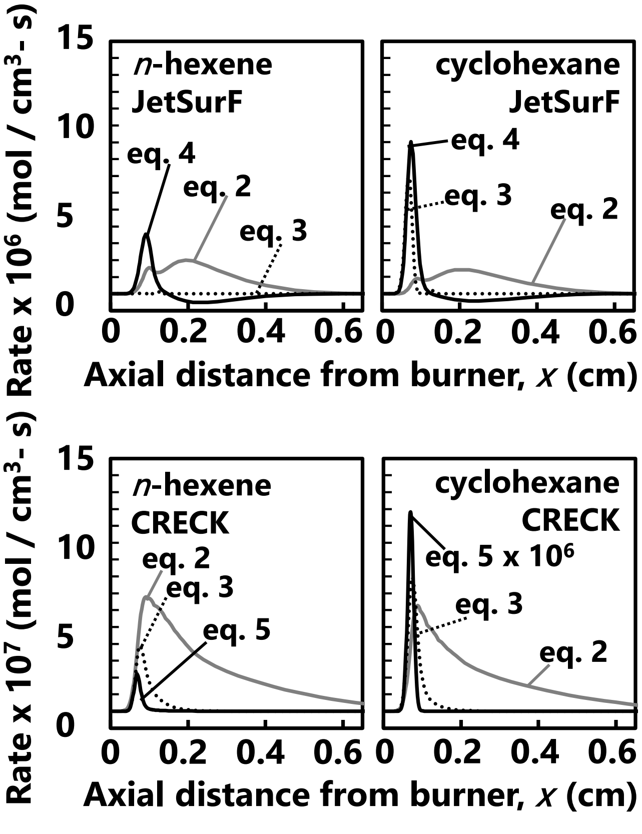

Figure 12: Reaction rate profiles computed for the three most productive benzene formation pathways based on the JetSurF model (top row) and CRECK PAH model (bottom row). The computation is based on the flame structure of the n-hexene (left column) and benzene (right column) flames at H_p = 1.2 cm.

Soot formation is not modeled in the current study, thus the predicted soot precursor concentrations are artificially high in the absence of soot. Validation of PAH chemistry in the absence of soot has recently been shown as a primary cause in discrepancies in existing soot formation models [48,64]. With this in mind, analysis of predicted gas-phase precursors is carried out only to compare the relative precursor chemistry among the current C6 hydrocarbon flames. PAH chemistry is examined by carrying out separate flame structure calculations based on the reduced CRECK PAH mechanism. This combustion chemistry model does not include oxidation chemistry for hexane and methylpentane so analysis is limited to the remaining fuels. The computed species profiles for small precursors and selected PAH are summarized Fig. 11 for the fuels included in the CRECK PAH mechanism. Fairly close agreement is observed for acetylene and propargyl production between the two models employed. A bigger discrepancy is observed for the predicted benzene production. Reasonable agreement occurs in the pre-heat zone, but a much higher concentration is predicted in the post-flame zone for the JetSurF computation. This may be due to a carbon equilibrium balance in the post-flame region tending towards higher benzene concentration in the absence of PAH in the JetSurF model. Both models predict a prominent peak of benzene production in the pre-heat region of the cyclohexane flame.

Naphthalene, lumped $C_{14}H_{10}$, and pyrene species profiles are also included in Fig. 11. The lumped $C_{14}H_{10}$ species represents phenanthrene, anthracene and homologous C_{13} and C_{15} [48]. Consideration of PAH allows for examination of the fate of benzene fuel. Namely, production of PAH in the preheat zone of the benzene flame indicates substantial pyrolysis to form stable PAH (and soot) before the flame front. Again, lower concentrations of soot precursors are predicted in the post-flame region of the benzene flame due to the lower equivalence ratio. With the exception of a moderate pre-flame peak of naphthalene, higher production of PAH is predicted for the n-hexene flame even though the flame is the same equivalence ratio and C/O ratio as the cyclohexane flame. The relatively fast onset of soot inception for cyclohexane relative to n-hexene may be related to the pre-flame production of benzene and naphthalene predicted.

Reaction rates are compared between the two combustion chemistry models in terms of benzene formation pathways. Upon examination, three pathways dominate benzene formation in both models. These include well established C_2 and C_3 paths based on acetylene and propargyl precursors. The third pathway to benzene is based on dehydrogenation of a non-aromatic C6 ring. These reactions are as follows:

$$2C_3H_3 = C_6H_6 \quad (2)$$

$$C_4H_5 + C_2H_2 = C_6H_6 + H \quad (3)$$

$$c\text{-}C_6H_7 = C_6H_6 + H \quad (4)$$

$$c\text{-}C_6H_8 = C_6H_6 + H_2 \quad (5)$$

Propargyl recombination (eq. 2) and butynyl + acetylene (eq.3) pathways are shared across the two models, but there is a slight difference in the treatment of dehydrogenation. JetSurF considers dehydrogenation from a ring of C_6H_7 whereas the

CRECK mechanism considers a C_6H_8 ring. Profiles of the reaction rate for the three pathways are shown in Fig. 12 for the two kinetic mechanisms. The two models both consider combustion chemistry of n-hexene and cyclohexane, therefore, analysis of these flames provides a robust examination of fuel-specific and model-specific reaction rates. Distinctions are observed in rate profiles among the two kinetic models. Production in benzene by propargyl recombination is predicted to occur after the flame in the JetSurF model whereas the reaction is fastest at the flame front for CRECK. The combination of butynyl and acetylene to form benzene is significant for both fuels in the CRECK mechanism but this pathway is only active for cyclohexane in the JetSurF calculation.

The most significant fuel specific pathway to benzene in the *n*-hexene and cyclohexane flames is dehydrogenation. This is a pyrolysis process to form benzene in the pre-heat zone in flames for both fuels but cyclohexane flames are predicted to form benzene much faster than *n*-hexene. The early onset of soot inception in the cyclohexane flame may be related to the predicted dehydrogenation process in the pre-heat zone. Fairly close agreement exists for the predicted dehydrogenation rate in the cyclohexane flame across the two mechanisms. In contrast, the predicted rate of benzene formation for the other two pathways is an order of magnitude slower for the CRECK mechanism. Further quantification of discrepancies between the mechanisms is limited by the lack of benzene and PAH concentration measurements. However, the current computational analysis of species profiles and reaction rates is consistent with the observed evolution in measured soot mobility size distributions. Namely, pyrolysis reactions of cyclohexane and benzene fuels to form benzene and PAH in the pre-heat zone may contribute to the observed onset of soot inception.

4. Conclusions

The time resolved formation of soot from inception to later growth stages is examined for premixed burner stabilized stagnation (BSS) flames of C6 hydrocarbons. The measurements presented are valuable for combustion and fuels science community efforts to characterize soot formation using surrogate fuel approaches or models for real fuels. Surrogate fuels are formulated based on cumulative behavior of a small subset of fuels whereas real fuel studies consider the lumped behavior of a complex mixture. The current systematic study provides a basis for understanding soot formation behavior in flames from parent fuels representing alkanes, alkenes, cycloalkanes and aromatic structures. As such, the study of specific C_6 fuels aids surrogate development or the broad representation fuel functional groups could aid real fuel combustion models. The C_6 hydrocarbon family is the smallest set for which this comparison is possible.

The overall sooting process is comparable in the fuels as evidenced by similar time resolved bimodal mobility PSDF. However, the onset of particle inception and the persistence of nucleation-sized particles are dependent upon the structure of the parent fuel. The fastest onset of soot is observed in cyclohexane and benzene flames and this may be due to significant aromatic formation at the pre-flame region predicted by two separate combustion chemistry models. The observed PSDF evolution for cyclohexane and benzene flames also shows a transition to a single mode of growth-sized particles over time. The measured size distributions are based on particle mobility sizing which requires assumptions or knowledge of the particle morphology to properly interpret the measured mobility diameter. Atomic force microscopy characterization indicates that aggregates are formed across most of the size range and the particle morphology is similar for particle sampled from the n-hexane and benzene flames. Even for contrasting hydrogen saturation in the parent fuels, the measured particle cross-sectional area and sphericity are effectively equivalent for particles formed in these flames. Error associated with improper application of the spherical particle assumption is evaluated by applying simple aggregate mechanisms for the measured mobility diameter. The spherical assumption does not impact the PSDF number density result but the inferred volume fraction for aggregates deviates by up to an order of magnitude depending on the morphology assumptions adopted. The current work provides fundamental insights into soot formation affected by fuel molecular structure for a wide range of hydrogen saturation and carbon bonding. Subtle differences are expected from premixed flames but the application of detailed combustion chemistry mechanisms allows for examination of the effect of precursor formation pathways unique to each parent fuel structure. The current application of a detailed chemistry model in the context of soot formation behavior in n-hexane flames is particularly rare.

Conflicts of interest

There are no conflicts to declare

Acknowledgements

We are grateful to Dr. Enoch Dames for the helpful discussions regarding chemistry within the fuels studied and for supplying the reduced JetSurF mechanism. Prof. Hai Wang and Dr. Sydnie Lieb were involved in preliminary experimental work and discussions.

References

[1] J.B. Heywood, Internal Combustion Engine Fundamentals, McGraw-Hill, New York, 2018.

[2] I.M. Kennedy, The health effects of combustion-generated aerosols, Proc. Combust. Inst. 31 (2007) 2757–2770. https://doi.org/https://doi.org/10.1016/j.proci.2006.08.116.

[3] M.Z. Jacobson, Strong radiative heating due to the mixing state of black carbon in atmospheric aerosols, Nature. 409 (2001) 695–697. https://doi.org/10.1038/35055518.

[4] F.N. Egolfopoulos, N. Hansen, Y. Ju, K. Kohse-Höinghaus, C.K. Law, F. Qi, Advances and challenges in laminar flame experiments and implications for combustion chemistry, Prog.

Energy Combust. Sci. 43 (2014) 36–67. https://doi.org/https://doi.org/10.1016/j.pecs.2014.04.004.

[5] H. Wang, Formation of nascent soot and other condensed-phase materials in flames, Proc. Combust. Inst. 33 (2011) 41–67. https://doi.org/http://dx.doi.org/10.1016/j.proci.2010.09.009.

[6] C. Saggese, A. V. Singh, X. Xue, C. Chu, M.R. Kholghy, T. Zhang, J. Camacho, J. Giaccai, J.H. Miller, M.J. Thomson, C.-J. Sung, H. Wang, The distillation curve and sooting propensity of a typical jet fuel, Fuel. 235 (2019) 350–362. https://doi.org/10.1016/j.fuel.2018.07.099.

[7] W. Liu, X. Liang, A. Li, B. Lin, H. Lin, D. Han, Soot particle size distributions in premixed flames of RP-3 jet fuel and its distillates, Fuel. 267 (2020) 117244. https://doi.org/https://doi.org/10.1016/j.fuel.2020.117244.

[8] W. Liu, X. Liang, B. Lin, H. Lin, Z. Huang, D. Han, A comparative study on soot particle size distributions in premixed flames of RP-3 jet fuel and its surrogates, Fuel. 259 (2020) 116222. https://doi.org/https://doi.org/10.1016/j.fuel.2019.116222.

[9] W.D. Erickson, G.C. Williams, H.C. Hottel, Light scattering measurements on soot in a benzene□air flame, Combust. Flame. 8 (1964) 127–132. https://doi.org/https://doi.org/10.1016/0010-2180(64)90038-0.

[10] J.J. Macfarlane, F.H. Holderness, F.S.E. Whitcher, Soot formation rates in premixed C5 and C6 hydrocarbon□air flames at pressures up to 20 atmospheres, Combust. Flame. 8 (1964) 215–229. https://doi.org/https://doi.org/10.1016/0010-2180(64)90067-7.

[11] A. Ciajolo, A. Tregrossi, M. Mallardo, T. Faravelli, E. Ranzi, Experimental and kinetic modeling study of sooting atmospheric-pressure cyclohexane flame, Proc. Combust. Inst. 32 (2009) 585–591. https://doi.org/https://doi.org/10.1016/j.proci.2008.06.170.

[12] M. Alfè, B. Apicella, R. Barbella, A. Tregrossi, A. Ciajolo, Similarities and dissimilarities in n-hexane and benzene sooting premixed flames, Proc. Combust. Inst. 31 (2007) 585–591. https://doi.org/https://doi.org/10.1016/j.proci.2006.07.187.

[13] J. Thomas Mckinnon, J.B. Howard, The roles of pah and acetylene in soot nucleation and growth, Symp. Combust. 24 (1992) 965–971. https://doi.org/https://doi.org/10.1016/S0082-0784(06)80114-1.

[14] C. Russo, M. Alfè, J.-N. Rouzaud, F. Stanzione, A. Tregrossi, A. Ciajolo, Probing structures of soot formed in premixed flames of methane, ethylene and benzene, Proc. Combust. Inst. 34 (2013) 1885–1892. https://doi.org/https://doi.org/10.1016/j.proci.2012.06.127.

[15] J. Zhai, W. Liu, B. Lin, H. Lin, Z. Huang, D. Han, Size Distribution of Nascent Soot in Premixed n-Hexane, Cyclohexane, and Methylcyclohexane Flames, Energy & Fuels. 33 (2019) 5740–5748. https://doi.org/10.1021/acs.energyfuels.9b00904.

[16] M.M. Maricq, A comparison of soot size and charge distributions from ethane, ethylene, acetylene, and benzene/ethylene premixed flames, Combust. Flame. 144 (2006) 730–743. https://doi.org/http://dx.doi.org/10.1016/j.combustflame.2005.09.007.

[17] A.D. Abid, E.D. Tolmachoff, D.J. Phares, H. Wang, Y. Liu, A. Laskin, Size distribution and morphology of nascent soot in premixed ethylene flames with and without benzene doping, Proc. Combust. Inst. 32 (2009) 681–688. https://doi.org/https://doi.org/10.1016/j.proci.2008.07.023.

[18] C.A. Echavarria, A.F. Sarofim, J.S. Lighty, A. D’Anna, Modeling and measurements of size distributions in premixed ethylene and benzene flames, Proc. Combust. Inst. 32 (2009) 705–711. https://doi.org/https://doi.org/10.1016/j.proci.2008.06.172.

[19] C.A. Echavarria, A.F. Sarofim, J.S. Lighty, A. D’Anna, Evolution of soot size distribution in premixed ethylene/air and ethylene/benzene/air flames: Experimental and modeling study, Combust. Flame. 158 (2011) 98–104. https://doi.org/https://doi.org/10.1016/j.combustflame.2010.07.021.

[20] W. Liu, J. Zhai, B. Lin, H. Lin, D. Han, Soot size distribution in lightly sooting premixed flames of benzene and toluene, Front. Energy. 14 (2020) 18–26. https://doi.org/10.1007/s11708-020-0663-6.

[21] M. Sirignano, A. Ciajolo, A. D’Anna, C. Russo, Particle formation in premixed ethylene-benzene flames: An experimental and modeling study, Combust. Flame. 200 (2019) 23–31. https://doi.org/https://doi.org/10.1016/j.combustflame.2018.11.006.

[22] A.D. Abid, J. Camacho, D.A. Sheen, H. Wang, Quantitative measurement of soot particle size distribution in premixed flames - The burner-stabilized stagnation flame approach, Combust. Flame. 156 (2009) 1862–1870.

[23] A.D. Abid, J. Camacho, D. a. Sheen, H. Wang, Evolution of Soot Particle Size Distribution Function in Burner-Stabilized Stagnation n -Dodecane−Oxygen−Argon Flames, Energy & Fuels. 23 (2009) 4286–4294. https://doi.org/10.1021/ef900324e.

[24] J.P. Cain, J. Camacho, D.J. Phares, H. Wang, A. Laskin, Evidence of aliphatics in nascent soot particles in premixed ethylene flames, Proc. Combust. Inst. 33 (2011) 533–540.

[25] J. Camacho, S. Lieb, H. Wang, Evolution of size distribution of nascent soot in n- and i-butanol flames, Proc. Combust. Inst. 34 (2013) 1853–1860.

[26] J. Camacho, C. Liu, C. Gu, H. Lin, Z. Huang, Q. Tang, X. You, C. Saggese, Y. Li, H. Jung, L. Deng, I. Wlokas, H. Wang, Mobility size and mass of nascent soot particles in a benchmark premixed ethylene flame, Combust. Flame. 162 (2015). https://doi.org/10.1016/j.combustflame.2015.07.018.

[27] C. Gu, H. Lin, J. Camacho, B. Lin, C. Shao, R. Li, H. Gu, B. Guan, Z. Huang, H. Wang, Particle size distribution of nascent soot in lightly and heavily sooting premixed ethylene flames, Combust. Flame. 165 (2016) 177–187. https://doi.org/10.1016/j.combustflame.2015.12.002.

[28] H. Lin, C. Gu, J. Camacho, B. Lin, C. Shao, R. Li, H. Gu, B. Guan, H. Wang, Z. Huang, Mobility size distributions of soot in premixed propene flames, Combust. Flame. 172 (2016). https://doi.org/10.1016/j.combustflame.2016.07.002.

[29] K. V. Puduppakkam, J. Camacho, A.U. Modak, H. Wang, C. V. Naik, E. Meeks, A soot chemistry model that captures fuel effects, in: Proc. ASME Turbo Expo, 2014. https://doi.org/10.1115/GT2014-27123.

[30] C. Saggese, S. Ferrario, J. Camacho, A. Cuoci, A. Frassoldati, E. Ranzi, H. Wang, T. Faravelli, Kinetic modeling of particle size distribution of soot in a premixed burner-stabilized stagnation ethylene flame, Combust. Flame. 162 (2015). https://doi.org/10.1016/j.combustflame.2015.06.002.

[31] E.K.Y. Yapp, D. Chen, J. Akroyd, S. Mosbach, M. Kraft, J. Camacho, H. Wang, Numerical simulation and parametric sensitivity study of particle size distributions in a burner-stabilised stagnation flame, Combust. Flame. 162 (2015) 2569–2581. https://doi.org/10.1016/j.combustflame.2015.03.006.

[32] C. Saggese, A. Cuoci, A. Frassoldati, S. Ferrario, J. Camacho, H. Wang, T. Faravelli, Probe effects in soot sampling from a burner-stabilized stagnation flame, Combust. Flame. 167 (2016). https://doi.org/10.1016/j.combustflame.2016.02.013.

[33] C.R. Shaddix, Correcting thermocouple measurements for radiation loss: A critical review, 33rd Natl. Heat Transf. Conf. NHTC'99. (1999) 990805.

[34] B. Zhao, Z. Yang, J. Wang, M. V Johnston, H. Wang, Analysis of Soot Nanoparticles in a Laminar Premixed Ethylene Flame by Scanning Mobility Particle Sizer, Aerosol Sci. Technol. 37 (2003) 611–620. https://doi.org/10.1080/02786820300908.

[35] J. Camacho, Y. Tao, H. Wang, Kinetics of nascent soot oxidation by molecular oxygen in a flow reactor, Proc. Combust. Inst. 35 (2015) 1887–1894.

[36] J. Camacho, A. V. Singh, W. Wang, R. Shan, E.K.Y. Yapp, D. Chen, M. Kraft, H. Wang, Soot particle size distributions in premixed stretch-stabilized flat ethylene-oxygen-argon flames, Proc. Combust. Inst. 36 (2017) 1001–1009. https://doi.org/10.1016/j.proci.2016.06.170.

[37] J. Bonpua, Y. Yagües, A. Aleshin, S. Dasappa, J. Camacho, Flame temperature effect on sp2 bonds on nascent carbon nanoparticles formed in premixed flames (T > 2100 K): A Raman spectroscopy and particle mobility sizing study, Proc. Combust. Inst. 37 (2019) 943–951. https://doi.org/10.1016/j.proci.2018.06.124.

[38] S. Dasappa, J. Camacho, Thermodynamic barrier to nucleation for manganese oxide nanoparticles synthesized by high-temperature gas-to-particle conversion, Energy & Fuels. 32 (2021) 1874–1884.

[39] S. Dasappa, J. Camacho, Evolution in size and structural order for incipient soot formed at flame temperatures greater than 2100 Kelvin, Fuel. (2021).

[40] Z. Li, H. Wang, Thermophoretic force and velocity of nanoparticles in the free molecule regime, Phys. Rev. E. 70 (2004) 21205. https://doi.org/10.1103/PhysRevE.70.021205.

[41] Z. Li, H. Wang, Drag force, diffusion coefficient, and electric mobility of small particles. II. Application, Phys. Rev. E. 68 (2003) 61207. https://link.aps.org/doi/10.1103/PhysRevE.68.061207.

[42] A.E. Lutz, R.J. Kee, J.F. Grcar, F.M. Rupley, OPPDIF: A Fortan program for computing opposed-flow diffusion flames, (1997).

[43] C. Liu, J. Camacho, H. Wang, Phase Equilibrium of TiO2 Nanocrystals in Flame-Assisted Chemical Vapor Deposition, ChemPhysChem. 19 (2018) 180–186. https://doi.org/10.1002/cphc.201700962.

[44] S. Dasappa, J. Camacho, Formation of nanocrystalline manganese oxide in flames: oxide phase governed by classical nucleation and size-dependent equilibria, CrystEngComm. 22 (2020) 5509–5521. https://doi.org/10.1039/D0CE00734J.

[45] H. Wang, E. Dames, B. Sirjean, D.A. Sheen, R. Tango, A. Violi, J.Y.. Lai, F.N. Egolfopoulos, D.. Davidson, R.K. Hanson, C.T. Bowman, C.K. Law, W. Tsang, N.. Cernansky, D.. Miller, R.P. Lindstedt, A high-temperature chemical kinetic model of n-alkane (up to n-dodecane), cyclohexane, and methyl-, ethyl-, n-propyl and n-butyl-cyclohexane oxidation at high temperatures, JetSurF version 2.0, Http://Web.Stanford.Edu/Group/Haiwanglab/JetSurF/JetSurF2.0/Index.Html. (2010).

[46] L. Waldmann, Uber Die Kraft Eines Inhomogenen Gases Auf Kleine Suspendierte Kugeln, Zeitschrift Fur Naturforsch. 14 (1959) 589–599.

[47] E. RANZI, A. FRASSOLDATI, A. STAGNI, M. PELUCCHI, A. CUOCI, T. FARAVELLI, Reduced Kinetic Schemes of Complex Reaction Systems: Fossil and Biomass-Derived Transportation Fuels, Int. J. Chem. Kinet. 46 (2014) 512–542. https://doi.org/https://doi.org/10.1002/kin.20867.

[48] W. Pejpichestakul, E. Ranzi, M. Pelucchi, A. Frassoldati, A. Cuoci, A. Parente, T. Faravelli, Examination of a soot model in premixed laminar flames at fuel-rich conditions, Proc. Combust. Inst. 37 (2019) 1013–1021. https://doi.org/https://doi.org/10.1016/j.proci.2018.06.104.

[49] C.K. Law, Combustion Physics, Cambrige Press, Cambridge, 2006.

[50] H. Böhm, D. Hesse, H. Jander, B. Lüers, J. Pietscher, H.G.G. Wagner, M. Weiss, The influence of pressure and temperature on soot formation in premixed flames, Symp. Combust. 22 (1989) 403–411. https://doi.org/https://doi.org/10.1016/S0082-0784(89)80047-5.

[51] W.C. Hinds, Aerosol Technology: Properties, behavior and measurement of airborne particles, Wiley, New York, 1982.

[52] P. Meakin, Fractal aggregates, Adv. Colloid Interface Sci. 28 (1987) 249–331. https://doi.org/https://doi.org/10.1016/0001-8686(87)80016-7.

[53] M.L. Eggersdorfer, S.E. Pratsinis, The Structure of Agglomerates Consisting of Polydisperse Particles, Aerosol Sci. Technol. 46 (2012) 347–353. https://doi.org/10.1080/02786826.2011.631956.

[54] M. Schenk, S. Lieb, H. Vieker, A. Beyer, A. Gölzhäuser, H. Wang, K. Kohse-Höinghaus, Imaging Nanocarbon Materials: Soot Particles in Flames are Not Structurally Homogeneous, ChemPhysChem. 14 (2013) 3248–3254. https://doi.org/10.1002/cphc.201300581.

[55] G.A. Kelesidis, E. Goudeli, S.E. Pratsinis, Flame synthesis of functional nanostructured materials and devices: Surface growth and aggregation, Proc. Combust. Inst. 36 (2017) 29–50. https://doi.org/https://doi.org/10.1016/j.proci.2016.08.078.

[56] A.A. Lall, S.K. Friedlander, On-line measurement of ultrafine aggregate surface area and volume distributions by electrical mobility analysis: I. Theoretical analysis, J. Aerosol Sci. 37 (2006) 260–271. https://doi.org/https://doi.org/10.1016/j.jaerosci.2005.05.021.

[57] A.D. Abid, N. Heinz, E.D. Tolmachoff, D.J. Phares, C.S. Campbell, H. Wang, On evolution of particle size distribution functions of incipient soot in premixed ethylene–oxygen–argon flames, Combust. Flame. 154 (2008) 775–788. https://doi.org/https://doi.org/10.1016/j.combustflame.2008.06.009.

[58] P. Mitchell, M. Frenklach, Particle aggregation with simultaneous surface growth, Phys. Rev. E. 67 (2003) 61407. https://doi.org/10.1103/PhysRevE.67.061407.

[59] M. Balthasar, M. Frenklach, Detailed kinetic modeling of soot aggregate formation in laminar premixed flames, Combust. Flame. 140 (2005) 130–145. https://doi.org/https://doi.org/10.1016/j.combustflame.2004.11.004.

[60] K. Park, F. Cao, D.B. Kittelson, P.H. McMurry, Relationship between Particle Mass and Mobility for Diesel Exhaust Particles, Environ. Sci. Technol. 37 (2003) 577–583. https://doi.org/10.1021/es025960v.

[61] G.A. Kelesidis, S.E. Pratsinis, Determination of the volume fraction of soot accounting for its composition and morphology, Proc. Combust. Inst. (2020). https://doi.org/https://doi.org/10.1016/j.proci.2020.07.055.

[62] A. D’Anna, M. Commodo, P. Minutolo, Particle Inception in a Laminar Premixed Flame of Benzene, Combust. Sci. Technol. 180 (2008) 758–766. https://doi.org/10.1080/00102200801893754.

[63] F. TAKAHASHI, I. GLASSMAN, Sooting Correlations for Premixed Flames, Combust. Sci. Technol. 37 (1984) 1–19. https://doi.org/10.1080/00102208408923743.

[64] A. Veshkini, N.A. Eaves, S.B. Dworkin, M.J. Thomson, Application of PAH-condensation reversibility in modeling soot growth in laminar premixed and nonpremixed flames, Combust. Flame. 167 (2016) 335–352. https://doi.org/https://doi.org/10.1016/j.combustflame.2016.02.024.